# Electron beam transport analysis of W-band sheet beam klystron

Jian-Xun Wang,[1] Larry R. Barnett,[1] Neville C. Luhmann, Jr.,[1] Young-Min Shin,[1,a)] and Stanley Humphries[2]
[1]*Department of Applied Science, University of California, Davis, California 95616, USA*
[2]*Field Precision LLC, Albuquerque, New Mexico 87192, USA*

(Received 15 February 2010; accepted 11 March 2010; published online 22 April 2010)

The formation and transport of high-current density electron beams are of critical importance for the success of a number of millimeter wave and terahertz vacuum devices. To elucidate design issues and constraints, the electron gun and periodically cusped magnet stack of the original Stanford Linear Accelerator Center designed W-band sheet beam klystron circuit, which exhibited poor beam transmission ($\leq$55%), have been carefully investigated through theoretical and numerical analyses taking advantage of three-dimensional particle tracking solvers. The re-designed transport system is predicted to exhibit 99.76% (cold) and 97.38% (thermal) beam transmission, respectively, under space-charge-limited emission simulations. The optimized design produces the required high aspect ratio (10:1) sheet beam with 3.2 A emission current with highly stable propagation. In the completely redesigned model containing all the circuit elements, more than 99% beam transmission is experimentally observed at the collector located about 160 mm distant from the cathode surface. Results are in agreement of the predictions of two ray-tracing simulators, CST PARTICLE STUDIO and OMNITRAK which also predict the observed poor transmission in the original design. The quantitative analysis presents practical factors in the modeling process to design a magnetic lens structure to stably transport the elliptical beam along the long drift tube. © *2010 American Institute of Physics*. [doi:10.1063/1.3383053]

## I. INTRODUCTION

Recently, considerable attention has been focused on vacuum electronic devices (VEDs) as a breakthrough in powerful coherent radiation source development in the terahertz wave regime (~0.1 to 10 THz), owing to their high energy conversion efficiency and large thermal power capacity. In particular, sheet electron beam devices have been intensively investigated for high frequency electronic circuit applications as this increases output power and reduces beam current density proportional to the beam width, thereby allowing the use of low Brillouin magnetic fields, which permits the employment of permanent magnets in the electron beam focusing system. Furthermore, the two-dimensional geometry of the circuits provides compatibility with modern microelectromechanical systems fabrication technology, which enables affordable mass production of millimeter/submillimeter wave electronic circuits. Consequently, there is intense interest in the application of sheet beams to high frequency vacuum tubes for powerful RF generation. Early work on this topic tended to focus on analytic studies to understand the interaction mechanism and theoretical modeling to design circuits and magnetic lens structures,[1–4] followed by subsequent research on device construction. A W-band double vane traveling wave tube (TWT) amplifier with periodic permanent magnet (PPM) focusing has been investigated at the Los Alamos National Laboratory.[5] The Naval Research Laboratory has been developing a G-band (220 GHz) extended interaction klystron, which is designed to provide 453 W output with 41.6 dB gain from the 16.5 kV and 0.52 A electron beam, and a Ka-band coupled-cavity TWT.[6,7] Various other slow wave structures such as the staggered double vane array, grating, and photonic band gap have been also considered for sheet beam device application.[8–10] However, despite noticeable progress on these research activities, they have all encountered the critical issue of the high aspect ratio sheet beam formation and the need for high transmission efficiency transport.[11–13] A variety of approaches such as cylindrical/elliptical solenoids (with or without quadrupole magnets), wiggler field focusing, and periodically cusped magnet (PCM) configurations have thus been proposed and investigated with numerical and experimental analyses with an aim of achieving stable transport of a well focused sheet beam.[14–17]

Scheitrum and colleagues at the Stanford Linear Accelerator Center (SLAC) developed the magnetic lens taking advantage of a PCM array in conjunction with a W-band sheet beam klystron (WSBK) amplifier[18] program, which was intended to produce 50 kW peak power (2.5 kW average), with 40% efficiency and 40 dB gain, operating at 74 kV beam voltage and 3.6 A beam current with 12:1 aspect ratio.[19,20] With the assumption of a cathode temperature of $T_c$=1100 °K, beam current density of $J$=480 A/cm$^2$, and cathode emission current density of $J_c$=9 A/cm$^2$, the parametric calculations of Refs. 21 and 22 for the beam focusing conditions lead to a focusing magnetic field ($B_{\mathrm{rms}}$) of ~3.45 kG and maximum pole-to-pole distance ($L_{\mathrm{D}}$) of $\lesssim$1.65 cm, which is compatible with PCM focusing. A strong motivation for this work is the potential of the sheet beam klystron for use in portable terahertz radiation sources, with the multicavity WSBK appearing ideal for active denial

a)Electronic mail: ymshin@ucdavis.edu.

 

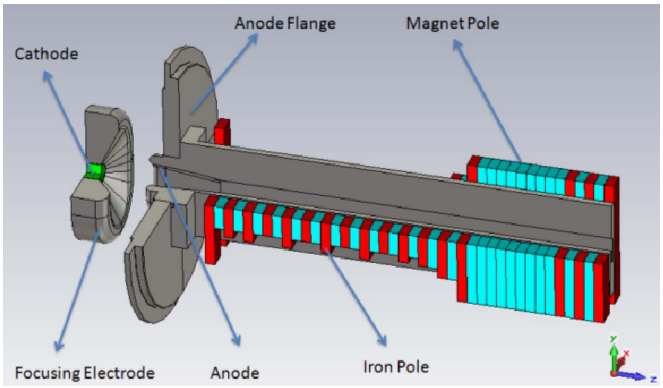


FIG. 1. (Color online) 3D model of the WSBK beam transport structure (electron gun, drift tube, and PCM).

system applications.[21] Theoretical and numerical analyses predicted the original WSBK design would produce more than 50 kW (2.5 kW average power) with 200 MHz instantaneous bandwidth. However, relatively poor beam transmission ($\leq$55%) was observed during experimental test of the proof-of-principle tube at SLAC. It was subsequently moved to UCD where extensive tests and tube optimization were performed which improved the transmission to 78% with ~11 kW output power, both of which fell far short of the simulation predictions. This motivated extensive theoretical and experimental investigations, from which the causes of the observed poor output performance were identified and which turned out to be both rf circuit problems and beam formation and transport problems. In the circuit category, it first turned out that the prototype had a poorly machined input cavity with inaccurate dimensions, which causes mode competition in the subsequent cavities. Also, the intermediate and penultimate cavities were slightly mistuned, so as to require mechanical tuners. Finally, the output cavity was shown to have mode competition problems resulting from period velocity-tapering and too many interaction gaps and a large amount of radiation energy is trapped in the stepped transition waveguide. Details of these problems together with three-dimensional (3D) PIC simulations verifying the features of the design of a new quasioptical output circuit and cavity design are provided in Ref. 22.

In addition to the rf circuit issues, considerable study was devoted to the sheet beam formation and transport which is the subject of this paper, the results of which have broad applicability beyond the WSBK. Figure 1(a) shows the 3D beam transport model, including the sheet beam electron gun and the PCM structure, of the prototype WSBK amplifier. In the beam area, the computer simulation analysis revealed that the PCM in the initial beam transport system was extremely sensitive to nonuniformities in the remanence magnetic flux density distribution, had misaligned pole-piece position, and also a nonoptimal cathode-PCM distance, all of which contributed to the observed poor beam transmission. Therefore, the entire beam focusing system, including the electron gun, drift tube, PCM structure, and collector, has been analyzed and redesigned by 3D magnetostatic/electrostatic solvers and particle tracking simulators.[23]

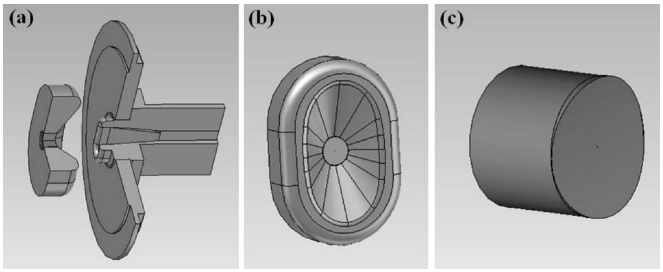


FIG. 2. Electron gun model. (a) 3D view. (b) FE. (c) Cylindrical cathode.

This paper presents the simulation models of the designed sheet beam structure and their static EM response corresponding to dimensional variations. The 3D spatial evolution and propagation dynamics of the magnetically focused electron beam is also analyzed with respect to the design parameters. Finally, thermal effects on the beam formation and transmission will be discussed in comparison with nonthermal electron beam analysis. For the simulation analysis, we employed three EM/particle simulators, MAXWELL-3D®,[24] CST PARTICLE STUDIO (PS)®,[25] and Field Precision OMNITRAK.[26]

## II. COMPARATIVE VERIFICATION OF SIMULATION MODELS

### A. Electron gun

The SLAC-designed electron gun forms the sheet beam following the paraxial-ray dynamics that the rectilinear-ray of the circular beam emitted from the curved cathode surface is squeezed by the potential pressure of the electrostatic optics and converted down to an elliptical beam. For the simulation analysis, two 3D simulators, CST-PS and OMNITRACK, were employed. The tracking solvers simply compute the particle trajectory through a precalculated electromagnetic field. In the finite-element-method (FEM) computation algorithm (CST-PS), the electric and magnetic fields are interpolated to the particle position with a linear interpolation scheme together with computing the current and space charge due to the particles. The gun-iteration consists of an iterative application of an electrostatic solver and a particle tracker. After calculating the electrostatic field, the particles are emitted and tracked and their space charge calculated. This space charge is used to modify the right hand side of the electrostatic solver (the charge-vector). Afterwards, a new electrostatic field is calculated which incorporates knowledge of the particles' flight path. This procedure is repeated until the relative difference of the emitted current and space charge meets a specified convergence criterion. Figure 2 illustrates the designed sheet beam gun model, which consists of a cylindrical cathode, a focus electrode (FE), anode, and a shielding flange. The FE and anode peripheries are initially designed from the equipotential distribution of the sheet beam structure following the basic electrostatics and their dimensions are precisely engineered to produce the maximum beam transmission at the anode tunnel exit. To provide adequate lifetime for the scandate cathode, the emission current density on the cathode surface is maintained at 9 $A/cm^2$

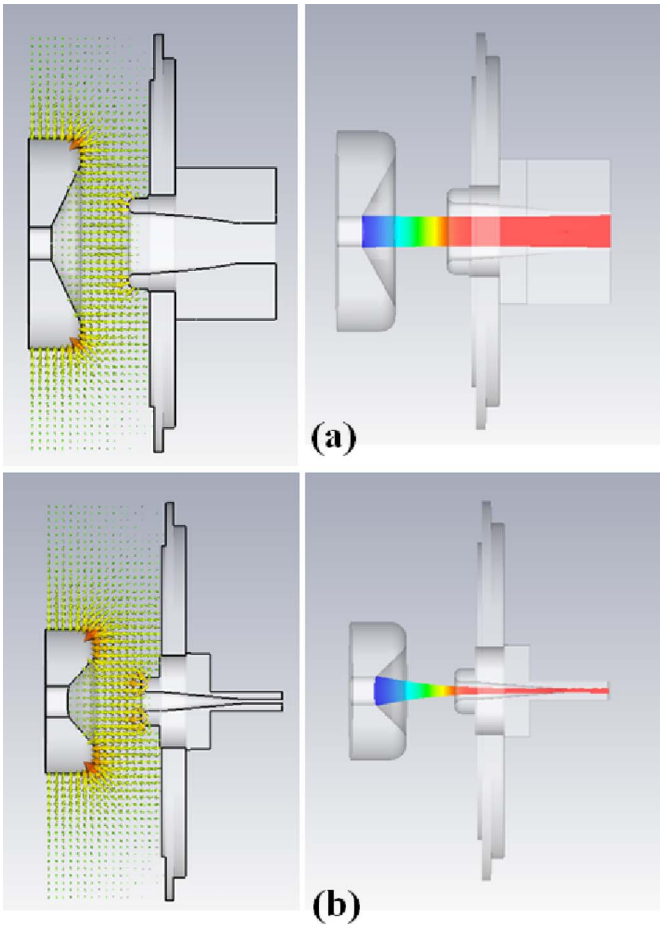


FIG. 3. (Color online) Electrostatic field vector plot (L) and spatial particle distribution (R) of the sheet beam gun (CST-PS). (a) Top view ($y$-$z$ plane); (b) side view ($x$-$z$ plane).

and the beam density rises to 90 $A/cm^2$ in the beam tunnel, corresponding to a 10:1 convergence ratio. The adaptive mesh refinement iteratively recomputes the static field distribution and macroparticle trajectory corresponding to an increasing number of meshes. The 20 steps of iteration converges the simulation result within $\geq -30$ dB accuracy, generating ~8.5 million hexagonal meshes ($\Delta x=100$ $\mu$m, $\Delta y=100$ $\mu$m, and $\Delta z=50$ $\mu$m near the cathode region) and 5322 particles. The cathode and focus electrode are biased at −74 kV and the anode is grounded. The transverse symmetric H-planes ($x$-$z$ and $y$-$z$) assign only a quarter of the entire gun model for simulation to save computational time. The periphery of the simulation box is set up with open boundaries to avoid spurious signal reflections. For the simulations, a workstation with a 3.16 GHz Intel Xeon CPU and 16 GB RAM was utilized for the computations.

The electric lens configuration is more clearly visualized in Fig. 3, showing the electric-field vector plot and the spatial electron distribution at the (a) $y$-$z$ and (b) $x$-$z$ planes. It is apparent that the static field distribution along the equipotential lines is densely localized around the sharp corners such as the anode nose and FE edge. The maximum electric-field strength is ~9.6 MV/m at the FE surface and ~8.9 MV/m at the anode, respectively. The field plot shows that the designed gun has a large vertical electric pressure, squeezing the circular beam into the thin elliptical sheet. Note in Fig. 3 that the beam size remains constant in the $y$-direction, whereas it is gradually compressed to the minimum waist in the $x$-direction. Figure 4 illustrates the cross-sectional particle distributions (CST-PS) at the distances, 0, 10, 20, and 30 mm, from the cathode surface, which clearly illustrates how the circular shape transforms down to the desired planar shape. The converged transmitted beam current, monitored at the end of anode hole, is ~3.16 A from CST-PS and ~3.24 A from OMNITRAK, respectively, which both agree well with the experimental data, 3.2 A, measured through the beam transmission test. In the simulation, electrons are defined as non-thermal ($T=0$) charged particles, so that the Landau damping effect within a Debye length is neglected in the cold plasma.

### B. PCM structure

To provide stable sheet beam focusing through the beam tunnelwidth a high filling factor in a W-band klystron module, the lens structure comprised of permanent magnets is considered owing to its compactness and efficiency. In particular, the PCM efficiently transports a high aspect ratio sheet beam in that the alternatively polarized magnet pole-piece stack produces strong transverse field components effectively suppressing lateral space charge forces. This magnet design enables the electron beam to avoid the diocotron instability,[2] which can occur in a constant solenoid field, resulting from the velocity shear ($\vec{E}\times\vec{B}$) across the top and bottom of the sheet beam, where $\hat{E}$ is the transverse space-charge electric field and $\hat{B}$ is the solenoid magnetic field. In

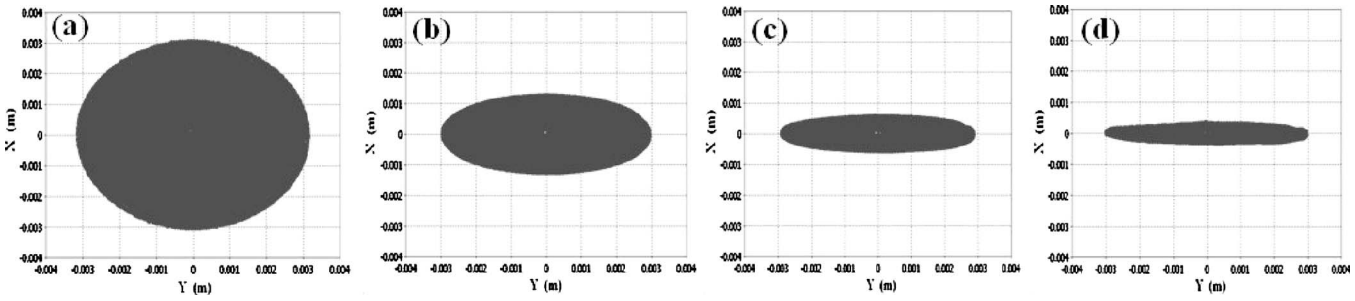


FIG. 4. 2D particle distributions at the cross-sectional planes (CST-PS) cathode surface, (b) $z=10$ mm, (c) $z=20$ mm, and (d) $z=30$ mm.

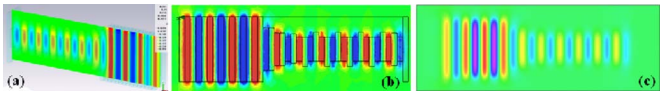


FIG. 5. (Color online) 2D axial magnetic field ($B_z$) distribution from (a) CST PARTICLE STUDIO, (b) MAXWELL3D, and (c) OMNITRAK.

general, the longitudinal magnetic field components off the axis are approximated from the on-axis field, $B_0$, as follows:[16]

$$B_{y,m}(y,z) \approx -B_0 \sinh(k_m y)\cos(k_m z), \tag{1}$$

$$B_{z,m}(y,z) \approx -B_0 \cosh(k_m y)\sin(k_m z), \tag{2}$$

where $k_m = 2\pi/\lambda_m$ and $\lambda_m$ is the spatial period of the magnet array. In the PCM structure, the off-axis staggered magnet pole-piece array provides the following fringe magnetic field components:

$$\begin{aligned} B_{x,s} = \frac{B_{s0}}{4\pi}\{&\ln[(x-x_m)^2+(y-y_m)^2] \\ &-\ln[(x-x_m)^2+(y+y_m)^2] \\ &-\ln[(x+x_m)^2+(y-y_m)^2] \\ &+\ln[(x+x_m)^2+(y+y_m)^2]\}, \end{aligned} \tag{3}$$

$$\begin{aligned} B_{y,s} = \frac{B_{s0}}{2\pi}\Bigg[&\tan^{-1}\left(\frac{x-x_m}{y-y_m}\right)-\tan^{-1}\left(\frac{x-x_m}{y+y_m}\right) \\ &+\tan^{-1}\left(\frac{x+x_m}{y-y_m}\right)-\tan^{-1}\left(\frac{x+x_m}{y+y_m}\right)\Bigg], \end{aligned} \tag{4}$$

giving rise to a side-focusing effect.

Based on the focusing mechanism of the planar configuration, the magnet system is designed to have a gradual transition from the PCM array to the long-period magnet (LPM) stack to ensure low emittance sheet beam propagation. Figure 5 shows axial magnetic field plots of the designed PCM models for the sheet beam transport in the W-band klystron in (a) CST-PS, (b) MAXWELL3D, and (c) OMNITRAK, which imports the original magnet model. All the simulators are set up to have the same magnet parameters: $B_r$(remanence magnetic fluxdensity)=1.1 T and $\mu_m$(relative permeability)=1.05, which are equivalent to samarium cobalt. The magnet stack contains 34 iron pole-pieces, defined as a nonlinear material in CST-PS and MAXWELL3D and a linear one in OMNITRAK. It turns out that the linearity of the magnetization does not significantly affect the simulation result. In the designed magnet model, the LPM array has a vertically magnetized magnet every two axially magnetized ones, whereas all the magnets and iron pole-pieces are magnetized in the axial direction in the PCM region. The insertion of vertically polarized magnet pieces into the LPM stack plays a role in enhancing the transverse field pressure, uniformly compressing the highly bunched electron beam with a larger space charge defocusing force at the output cavity. Figure 5 demonstrates the contour plots of the axial magnetic field ($B_z$), obtained from the three simulation codes, and they are seen to all have the identical

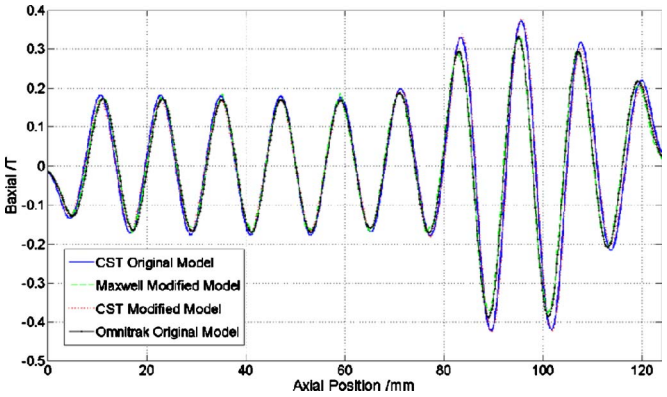


FIG. 6. (Color online) 1D distance vs axial magnetic field graph along the tunnel axis, obtained from CST-PS, MAXWELL3D, and OMNITRAK.

spatial distribution. It should be noted that the field plots show not only a sinusoidal varying axial magnetic field distribution but a distinct fringe field at both of the magnet edges. In Fig. 6, the $B_z$ versus axial position plots obtained from CST-PS, MAXWELL3D, and OMNITRAK are seen to agree well (within 0.1%), which verifies the designed sheet beam focusing system. The engineered magnet design with the round shape at the corners was simply modified as a rectangular geometry in the simulation model to reduce the number of meshes. Eventually, using the verified simulation modeling process, we identified the causes of the observed poor beam transmission and redesigned the original WSBK sheet beam transport system.

## III. IDENTIFICATION OF ORIGINAL WSBK SHEET BEAM TRANSPORT SYSTEM PROBLEMS AND SOLUTIONS

An entire beam transport simulation is extremely complicated and time-consuming as it includes all the curved circuit elements, such as the cathode, FE, anode, and flange, thereby significantly increasing the number of meshes with the consequence that simulation takes longer time to simultaneously compute the field distribution and particle trajectory with the adaptive mesh refinement procedure. Therefore, we divided the modeling process into two simulation routines: (a) magnet structure modeling and (b) particle tracking with electrostatic field calculation. As shown in Fig. 7, the magnet structure is first simulated in a separate computation and then its calculated 3D magnetostatic field profile is exported to the particle tracking simulator. This simulation method significantly reduces computation time and improves convergence capability since a magnet structure no longer occupies the drift tube, so that the simulation converges more rapidly with relatively fewer meshes. Also, it is no longer necessary to calculate magnetic fields corresponding to the magnet geometry together with the particle positions relevant to the electric-field distribution. For the simulation process, a full circuit model, not a quarter one, is considered as the imported field data are compatible with a full space.

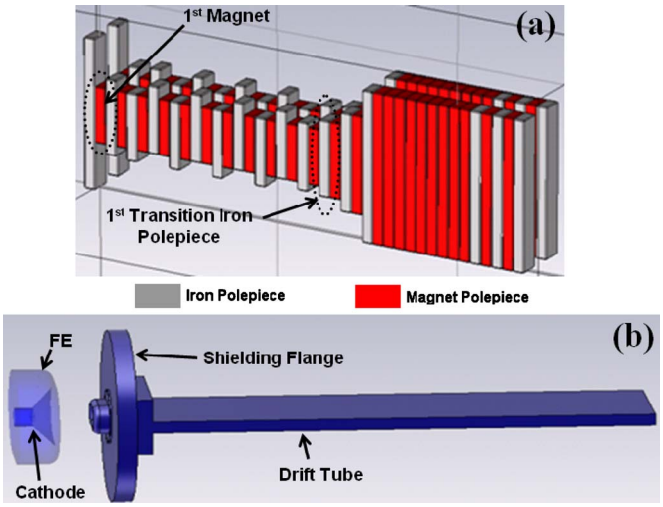


FIG. 7. (Color online) Beam transport system simulation sequence. (a) Focusing magnet model for magnetic field transfer to (b) electron-gun and drift-tube model.

### A. Mismatch of remanence flux density ($B_r$)

Using the simulation method, we analyzed the influence of a remanence flux density ($B_r$) mismatch between magnets on the beam transmission passing through the 120 mm long beam tunnel. In order to simplify the analysis conditions, we only swept the flux density of the first magnet, with the remaining magnets maintained at constant $B_r$. The inset in Fig. 8 illustrates the simulation model with the shielding flange, indicating the first magnet position. Figure 8 shows the effect of the mismatch ratio (magnetic flux density) between the first magnet and the others on the beam transmission. Note that the beam transmission is very high, almost 100%, under the no mismatch condition, whereas it rapidly decreases with an increase in the mismatch ratio. We experimentally measured the mismatch ratio of the original PCM stack and it turns out that all the magnets in the stack have ~7.5% mismatch on the average. In the transmission graph of Fig. 8, this mismatch ratio corresponds to a predicted beam transmission of ~78%, which is in remarkable agreement with the experimental beam transmission data. This result thus implies that the magnetic flux density is a crucial factor in determining the beam transmission. A PPM stack can be manufactured to have flux density uniformity of less than 2%, so that the beam transmission might be increased above 92% according to the graph. Current WSBK tube has the new magnet stack, which has only ±1–2% mismatch ratio. The leakage field strength in the electron gun area sensitively varies with respect to the magnetization amplitude of the first magnet pole-piece. Excessive leakage field would disturb the particle orbits and overly compress the electron rays resulting in severe scalloping. The original design had a nonmagnetized iron anode flange to shield the gun area. We thus investigated how the magnetic shielding affects the beam transmission. Figure 8(b) contains spatial beam transmission graphs in the axial direction of the two gun models with and without the anode shielding flange. According to the simulation result in the figure, it is obvious that the system has much higher beam transmission with the flange than that without one, which clearly shows that the leakage field arising from the first magnet is effectively eliminated by an iron shielding block. Therefore, a more uniform magnetic flux distribution (≤2%) along the magnet array with the anode shielding flange is included in the redesign process for the optimized beam transport system.

### B. Symmetric position of the transition pole-piece

The LPM is designed to be wider than the PCM to enhance the side potential pressure to cancel out the intense lateral space charge force of the strongly bunched electron beam. Thus, the original lens structure has a tapering transition section between the staggered pole-piece array and the line-aligned magnet array. In the early model, the first iron pole-piece was designed to be positioned off the center axis as an extension of the PCM structure, as shown in Fig. 7(a). However, the asymmetric position distorts the transverse

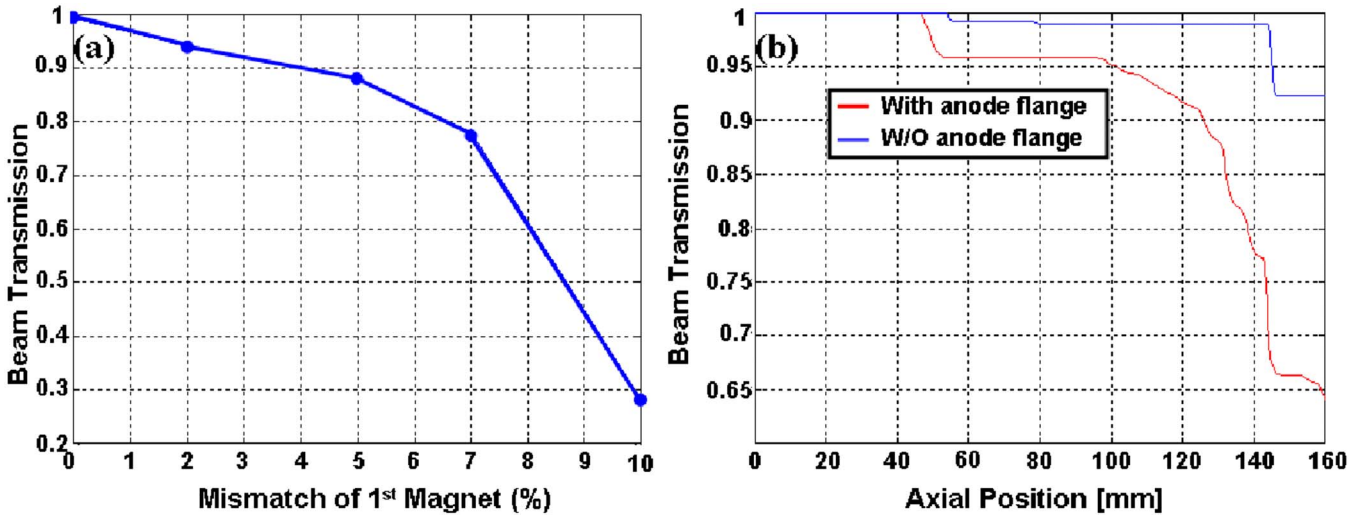


FIG. 8. (Color online) Remanence magnetic flux density (Br) vs beam transmission graph (b) distance vs beam transmission graphs with and without anode flange.

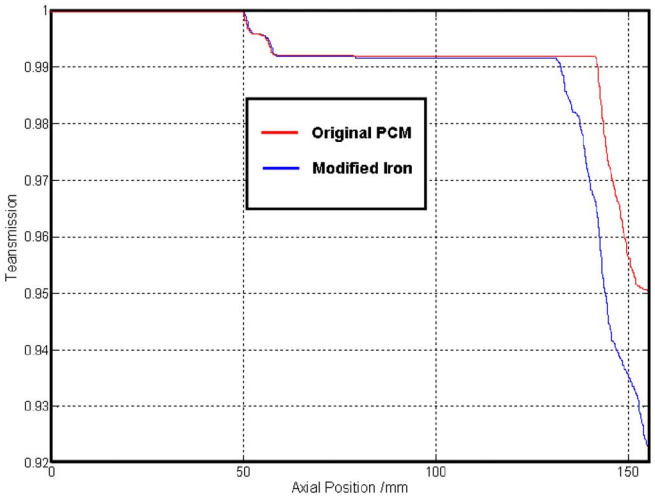


FIG. 9. (Color online) Distance vs beam transmission with asymmetric and symmetric positions of the 1st transition iron pole-piece.

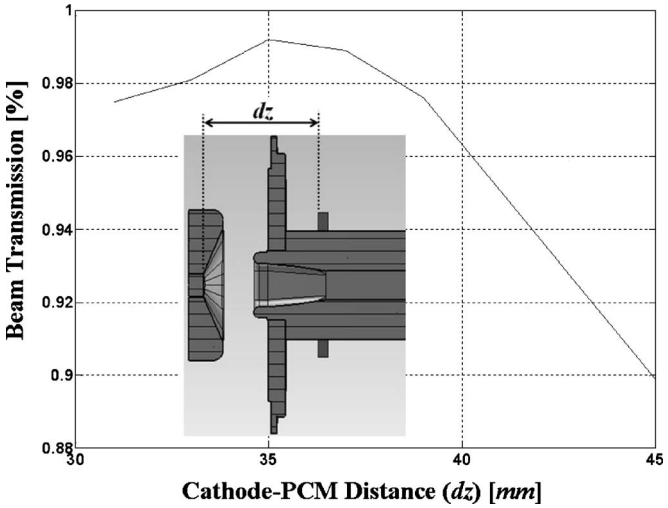


FIG. 10. Beam transmission graph with respect to distance between the cathode and the first iron pole-piece ($dz$) (inset is the illustration indicating the cathode-PCM distance).

field distribution slightly tilting the magnetic axis, which alters the flux path corresponding to the particle trajectory after the transition section. Figure 9 is the axial distance versus beam transmission graph simulated with the asymmetrically positioned pole-piece and the symmetrically positioned one. In the figure, high beam transmission ($\geq$99%) is maintained over a longer distance with the on-axis pole-piece ($\Delta z = \sim 140$ mm) than with the off-axis one ($\Delta z = \sim 130$ mm) at the end of the drift tube. According to the simulation result, the transverse position of the first pole-piece still affects the electron beam path, although it is not critical.

### C. Cathode-PCM distance

The axial PCM position relative to the cathode corresponds to the relative distance between the beam waist position and the first maximum $B_z$ position. In principle, the electron beam has a minimum ripple when the axial waist position is exactly matched with the axial $B_z$ (maximum) position. For a quantitative analysis, we thus monitored the variation in the beam transmission while sweeping the cathode-PCM distance. Figure 10 shows the distance versus beam transmission graph, which is monitored at the end of the beam tunnel, including the illustration in the inset. This simulation result displays the tradeoff between the transmission and cathode-PCM distance, increasing inversely proportional to the distance and falling after the maximum. The cathode-PCM distance was 45 mm in the original WSBK version, which is 10 mm away from the optimum position, 35 mm. According to the simulation result, the shift in the PCM position forward to 35 from 45 mm improves the beam transmission by 10%. The simulation results reveal that the transmission ratio can be significantly increased by optimizing the magnet position under the same design conditions. In the revised magnet structure, a cathode-PCM distance of 38 mm was selected as the optimum PCM position of 35 mm conflicts with other circuit components such as the input waveguide and the mechanical tuners.

### D. Completed WSBK beam transport system design

Finally, the design of the WSBK beam transport system is completed by considering the risk factors listed in A–C of Sec. IV, which led to poor beam transmission in the original circuit design. Figure 11 shows the magnetostatic and particle tracking simulation result of the optimized tube model: (a) axial magnetic field distribution ($B_z$) and (b) emitted beam trajectory. The transport system was modeled to include all of the circuit elements such as electron gun, shielding flange, drift tube, focusing magnet stack, and collector. In order to achieve reliable data with high accuracy, the designed circuit is modeled with more than 1 million meshes, which were specified by an adaptive mesh refinement process. The final design contains 2% remanence flux density uniformity, a symmetrically (on-axis) positioned transition iron pole-piece, and 38 mm cathode-PCM distance. Note that in Fig. 12, the sheet beam becomes gradually thinner as it propagates through the beam tunnel. The electron beam shown in Fig. 12(d) satisfies the initial design goal of 10:1 aspect ratio. Figure 13 is the spatial beam transmission of the designed circuit model. The simulation data show that almost all of the electrons completely pass through the drift tube while maintaining a high transmission rate of more than 99.6%. The drift tube model intended to ameliorate the existing problems demonstrated noticeably improved performance in that the electron beam transmission is increased by more than 20%. This simulation analysis was performed following a nonthermal ("cold") space-charge-limited (SCL) emission mechanism subject to Child–Langmuir law, so that

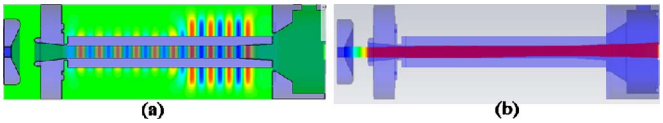


FIG. 11. (Color online) Simulation analysis result of completely designed WSBK transport system. (a) Static axial magnetic field ($B_z$) distribution. (b) Emitted beam trajectory.

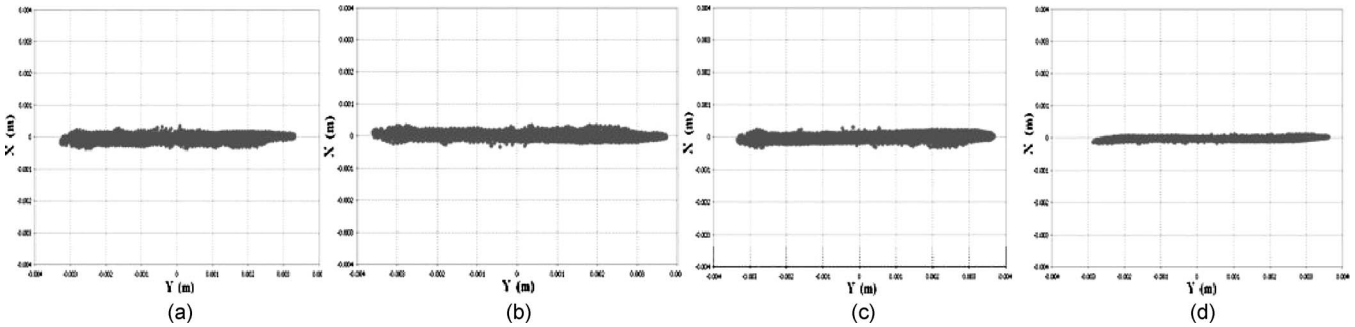


FIG. 12. Cross-sectional plots of particle distribution at the axial distance of (a) 20 mm, (b) 50 mm, (c) 80 mm, and (d) 110 mm.

we subsequently looked into the simulation result by considering thermal effects on the particle distribution which can adversely affect the transmission (Table I).

## IV. SHEET BEAM TRANSPORT OF THERMAL SCL EMISSION THROUGH NEW WSBK MODEL

The effects of cathode temperature are theoretically included in simulations of high-current, steady-state electron guns with the OMNITRAK code. Thermal distributions of transverse energy limit the performance of cylindrical guns with high compression ratio for generating small-diameter beams with high current density. Injection emittance also introduces limits in the performance of planar guns to generate narrow sheet beams for high-power microwave generation.[27] To represent the role of cathode temperature in the transverse electron dynamics of a SCL gun, one approach is to add small angular displacements to model particle orbits at the emission surface. The following method is used in the TRAK and OMNITRAK codes. The probability distribution of transverse velocity, $v_\perp$, of particles emitted from a source at temperature, $T_s$, approximates the Maxwell distribution:

$$f(\chi)d\chi = 2\chi \exp(-\chi^2)d\chi, \tag{5}$$

where

$$\chi = \sqrt{\frac{m}{2kT_s}}v_\perp. \tag{6}$$

The integral of Eq. (5) gives the cumulative probability, a variable in the range from 0 to 1:

$$\int_0^\chi f(\chi)d\chi = \mathrm{s} = 1 - \exp(-\chi^2). \tag{7}$$

The procedure in the codes is to generate a random value $0 \le \zeta \le 1$ and then to find a weighted value of $\chi$ from the inverse of Eq. (7):

$$\chi = -\frac{\ln(1-\zeta)}{2}. \tag{8}$$

The angle of the model particle relative to the local electric field is given by

$$\Delta\theta \cong \frac{v_\perp}{v_0} = \chi\sqrt{\frac{kT_s}{T_p}}, \tag{9}$$

where $T_p$ is the kinetic energy of the particle at the emission surface. Particles are emitted with a random distribution of azimuthal angle about the surface normal vector. The procedure is valid in the limit that $v_\perp \ll v_0$.

If all electrons created at the cathode are extracted ($j_s = j_c$), then we can identify the effective source temperature as the physical temperature of the cathode, $T_s = T_c$. Here, $j_s$ is the source current density, given by the Richardson–Dushman law, depending on the cathode material properties and temperature, and $j_c$ is the SCL current density, determined by the Child law which involves the properties of the extraction gap. It is important to recognize that $T_s$ may be lower than $T_c$ when $j_s > j_c$. The electron distribution at the cathode surface is Maxwellian with temperature $T_c$. When the source flux exceeds the Child-law value, a portion of the incident electrons must reflect back to the cathode. The depth of the potential barrier ensures that only a fraction of the available electron flux equal to $j_c$ passes. This fraction has the highest longitudinal energy and (on the average) a reduced transverse energy. Under typical operating conditions,

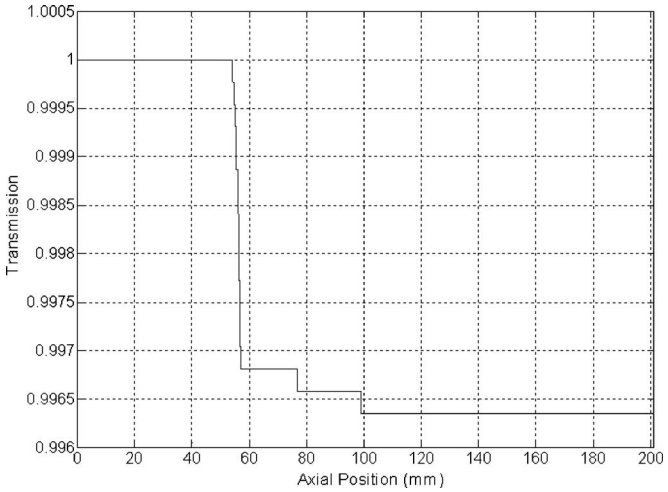


FIG. 13. Axial distance vs beam transmission graph of completely designed WSBK beam transport system from the electron gun to the collector. The monitored transmission is more than 99.6%.

TABLE I. Current and transmission.

| Temp (eV) | Current (A) | | | Transmission (%) | | |
|---|---|---|---|---|---|---|
| | Gun | Anode | Tunnel | Gun | Anode | Tunnel |
| 0 | 3.2328 | 3.2354 | 3.2277 | 99.89 | 99.76 | 99.69 |
| 0.4 | 3.2424 | 3.24 | 3.225 | 99.93 | 99.54 | 99.46 |
| 1.6 | 3.2364 | 3.2071 | 3.1231 | 99.09 | 97.38 | 96.5 |

the sheath is thin (a few micrometers) and therefore has a negligible effect on the value of $j_c$.[27] When $j_s > j_c$, the effective transverse temperature is lower than the cathode temperature through velocity selection at the extraction sheath. The result is somewhat counterintuitive. A small increase in the cathode temperature may result in a substantial reduction in the effective transverse temperature of the extracted beam.

Including the effects of cathode temperature on the beam emittance, we set up OMNITRAK simulations of planar beam transport with modified extraction channel dimensions, periodic magnet field configuration, and a full relativistic treatment of the gun. The beam propagated to the end of the anode extraction channel to a point just upstream of the magnet entrance. The beam distribution is then transferred to a second solution for propagation through the periodic magnet array with the relativistic approximation. For accurate modeling, the original computer-aided design drawings of the vacuum envelope, cathode support and cathode are imported to the code and their solid shapes are reconstructed by a basic mesh generator (METAMESH file). Starting from a cylinder of radius 3.16 mm, we cut the dished face with a convex extrusion that had the physical properties of vacuum. The mesh generator provides a good example of the use of part order, surface fitting commands, and coat commands to fit a complex region with multiple parts. The mesh with 1 623 664 elements represented the first quadrant in the cross-sectional ($x$-$y$) plane. Symmetric boundaries are assigned at $x=0$ mm and $y=0$ mm in the electric-field solution. An initial nonrelativistic calculation is made to generate an electric-field solution which included the effect of beam space charge. The field was used as input to full relativistic gun simulation. Three relativistic calculations are (1) zero transverse temperature at the emission surface, (2) a transverse temperature $T_s/e=T_c/4$, corresponding to a case where the spatial average of source current density is twice the Child-law current density, and (3) a transverse temperature $T_s=T_c$, the upper limit for thermal effects. A cathode temperature of 1423 °K corresponds to $kT_c/e \cong 0.16$ eV. For all cases, the code gave an injected current of 3.242 A. Figure

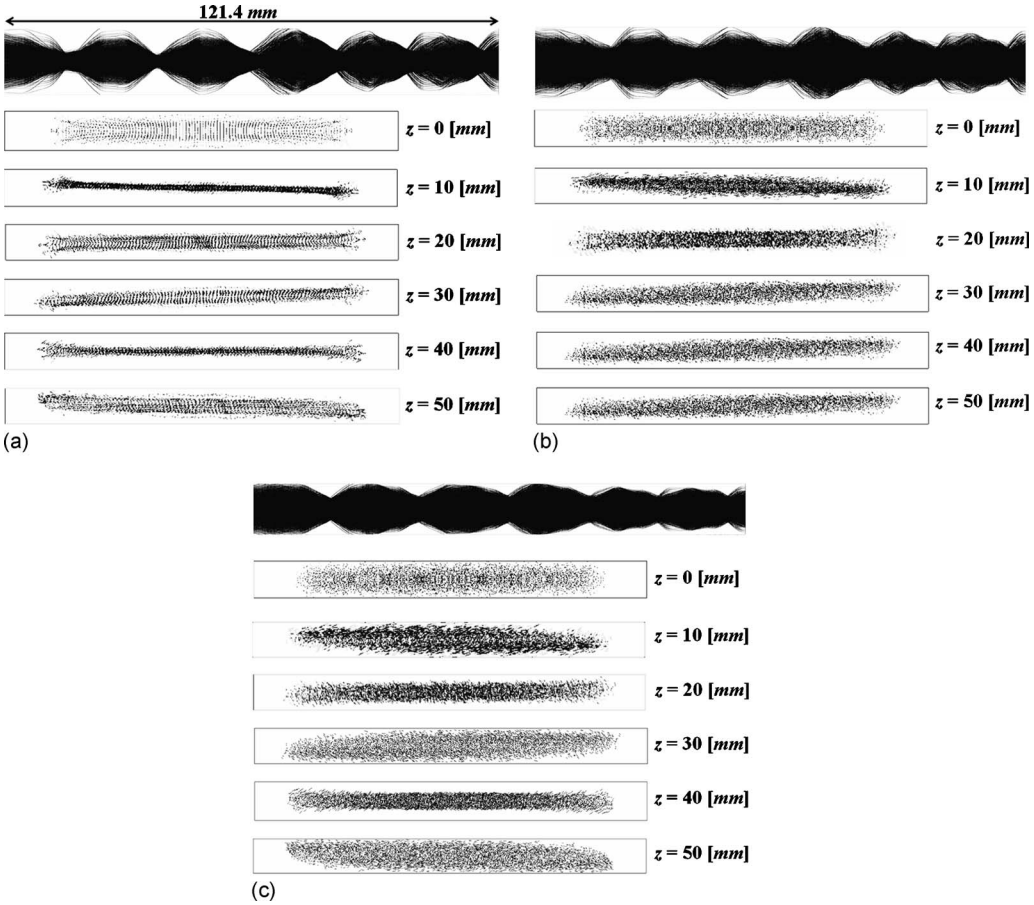


FIG. 14. Electron beam distributions in $x$-$z$ and $x$-$y$ planes at $z$=0, 10, 20, 30, 40, and 50 mm positions. (a) $T_s$=0.0 eV, (b) $T_s$=0.04 eV, and (c) $T_s$=0.16 eV.

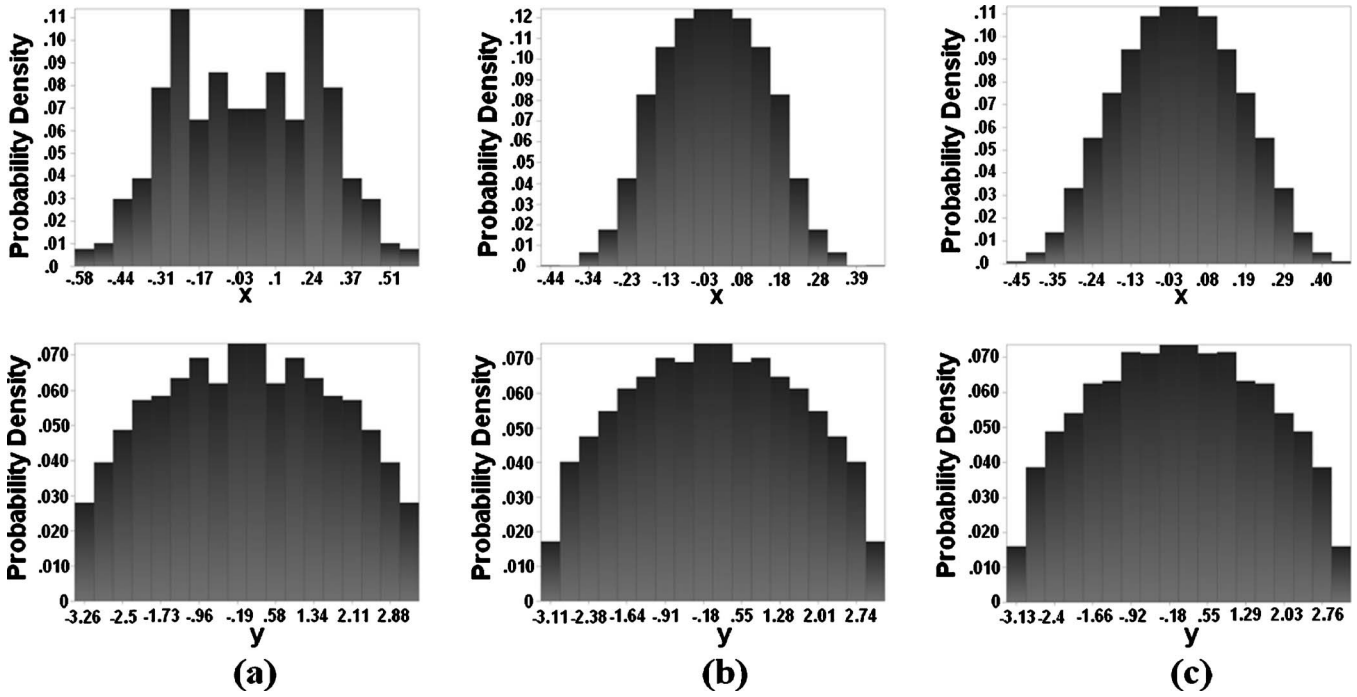


FIG. 15. Marginal probability distribution $F(x)$ in the $x$-direction (top) and $y$-direction (bottom). (a) $T_s=0.0$ eV, (b) $T_s=0.04$ eV, and (c) $T_s=0.16$ eV.

14 shows a plot of the model electron distribution in $x$-$y$ at the end of the anode structure. The axial location is just upstream from the focal point in the short direction Note that the scalloping magnitude tends to be reduced as the temperature increases, while the beam transmission is decreased. The initial beam temperature had a relatively small effect on the thickness in the short direction. This is also visible in Fig. 15, a plot of the marginal probability distribution, $F(z)=\int_0^\infty dy f(x,y)$. Figure 16 shows the phase-space distribution. Although there is little difference in the beam width in $x$, the cathode temperature strongly affected the distribution in angle $x'$. In all cases, the distribution has a negative average angle showing that the beam was slightly convergent just upstream from the magnet entrance.

The beam section tool is used to reflect electrons to fill the other three quadrants to prepare the beam distributions for the propagation solution. Through the beam transform tool, all particles are shifted by a distance $\Delta z=-14.4$ mm so that 1.4 mm upstream occurs from pole 1 in the coordinates of the magnetic field calculation. The solution for the beam-generated electric field is performed inside an axially uniform chamber with transverse dimensions $\Delta x=\pm 0.36$ mm and $\Delta y=\pm 4$ mm. The transmitted current, measured at $z=120$ mm, is 3.233 A for the cold beam and 3.224 A for the two thermal distributions. The transmission efficiency is better than 99.6%. Figure 17 shows the beam envelope from views normal to the long direction $(y)$ and the propagation axis $(z)$ for the solution with $T_s=T_c/4$. Figure 18 shows the short-direction phase-space distribution at the PPM exit $(z=120$ mm). The magnetic field strength clearly exceeded the match condition for the cold beam. The beam exhibited envelope oscillations and the nonlinear magnetic focusing forces increased the emittance. The high-temperature beam is almost matched in that the distribution maintained a constant shape as it propagated through the magnet stack. The end

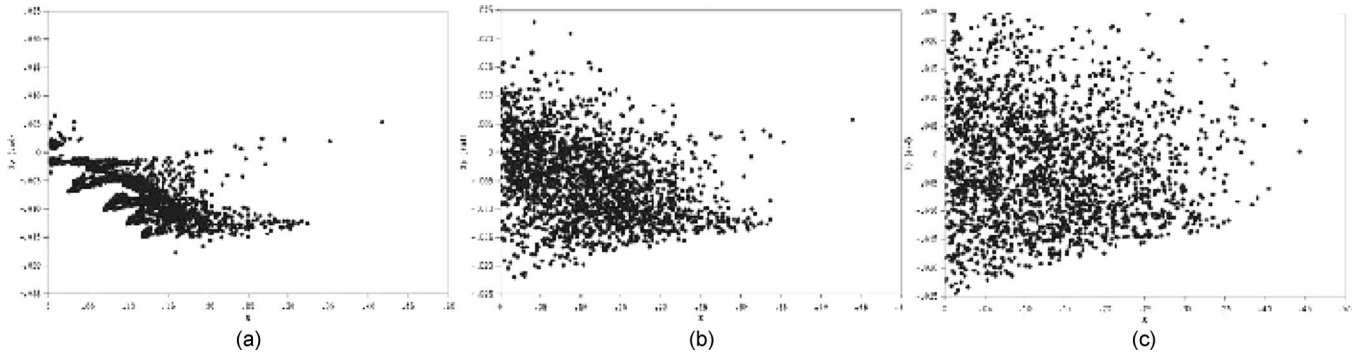


FIG. 16. Phase-space distribution $x$-$x'$ at a point 1.4 mm upstream from the face of pole 1. (a) $T_s=0.0$ eV, (b) $T_s=0.04$ eV, and (c) $T_s=0.16$ eV.

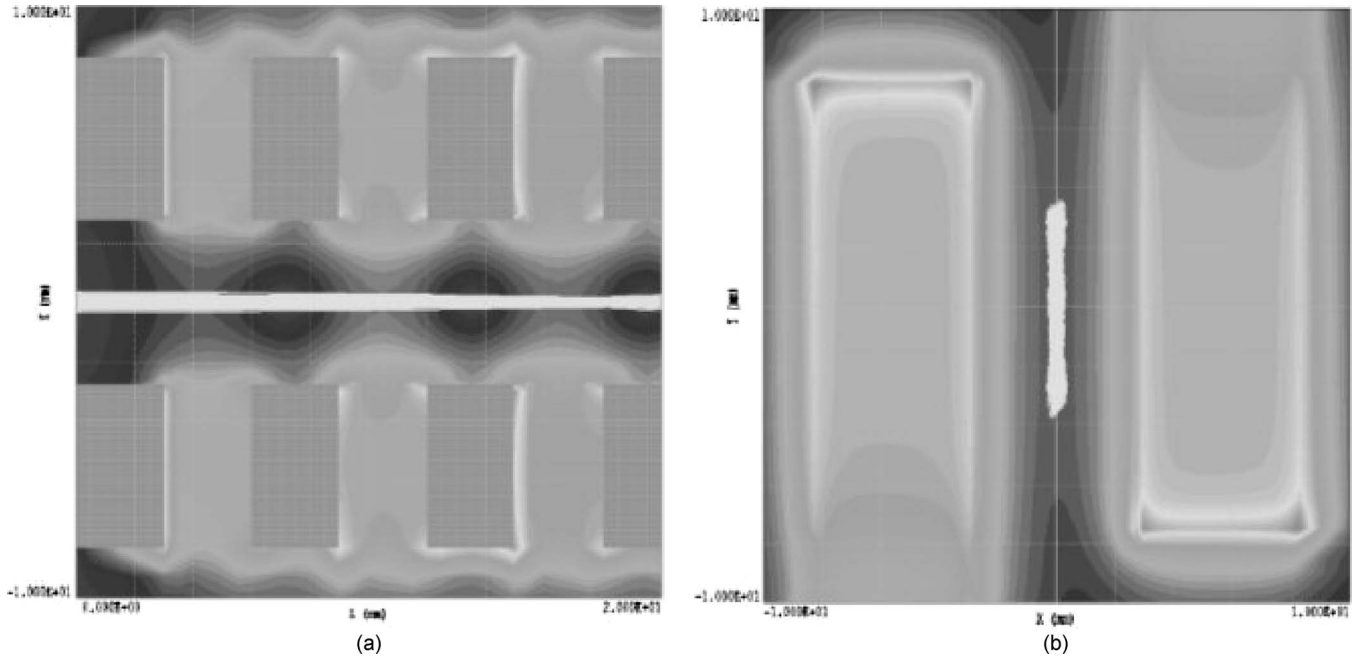

FIG. 17. (a) View normal to long direction ($y$) of the beam entering the magnet array, $T_s=T_c/4$ (b) view normal to the axis ($z$) showing the magnetic field amplitude near the magnet entrance and projections of electron orbits through the full transport system.

result is that the effective width of the high-temperature beam in the focusing was not significantly larger than that of the cold beam.

Finally, we have verified the simulation analysis (CST-PS and OMNITRAK) predictions through comparison with experimental data. Figure 19 shows beam transmission versus beam voltage in simulation and experiment. Experimental beam transmission is ~100% at the design voltage in good agreement with simulation. The major discrepancy is that the experimental result exhibits a voltage cutoff of beam transmission around 40 kV, while it appears around 20 kV in simulation. Note that thermionic emission simulation plot (OMNITRAK: thermionic emission) is more closely in agreement with experimental data, which implies that thermal dynamic motion of electrons in simulation has a strong effect on the beam voltage cutoff response. More data points would perhaps result in even closer coincidence between experiment and thermionic emission simulation. Furthermore, the discrepancy of low-voltage cutoff might be somewhat attributed to an artifact of imperfect alignment of the electron beam.

## V. CONCLUSION

Using static field solvers and ray-tracing codes, we have investigated and identified the problems with the original WSBK beam transport design. The FEM simulation analysis predicts that the revised design has a high transmission ($\geq$99.7%) of the high aspect ratio (10:1) planar beam through the tight beam tunnel under cold beam conditions.

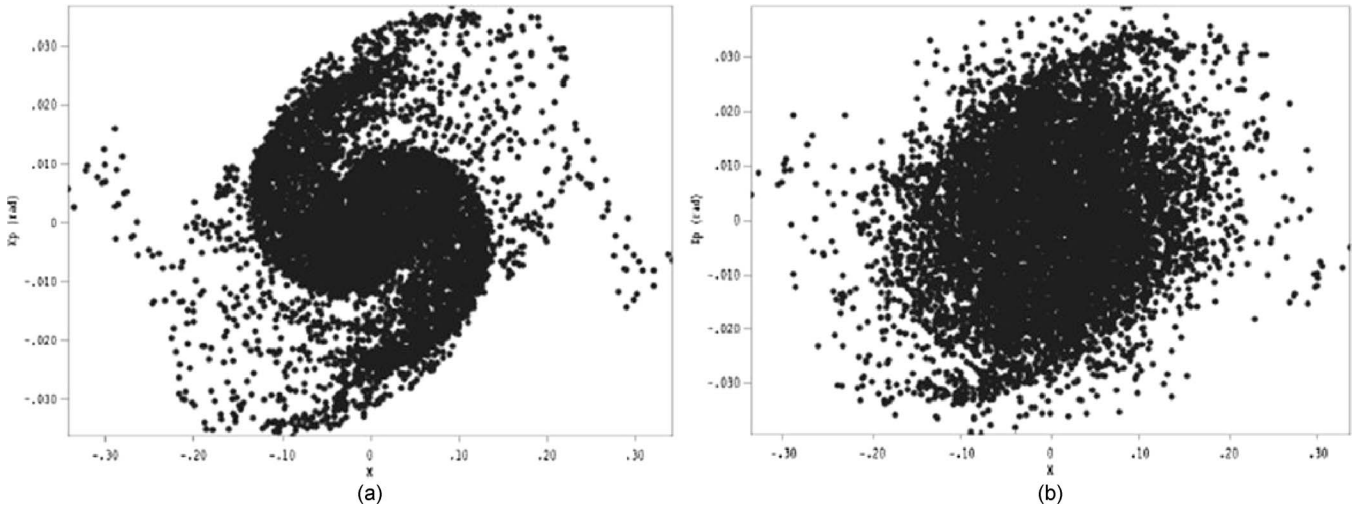

FIG. 18. Short-direction phase-space distributions ($x$-$x'$) at the end of the magnet stack ($z=120$ mm). (a) Cold beam. (b) $T_s=T_c$.

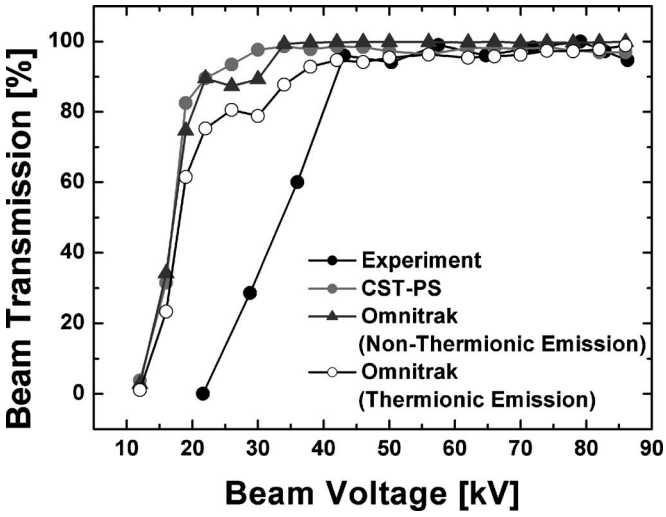


FIG. 19. Beam voltage vs transmission graphs obtained from experiment and simulation (CST-PS and OMNITRAK).

The numerical analysis accounting for thermal effects also predicts that the highly stable sheet beam focusing effect with a high transmission rate ($\geq$96.5%) of the designed model remains the same with a thermal distribution of electrons. Although the paper has described modeling of a specific gun and beam transport implementation, the results and insights are general and provide guidelines to systematically engineer a magnetic lens structure for other sheet beam VEDs in the millimeter and submillimeter wave regimes.

## ACKNOWLEDGEMENTS

This work is supported by the Marine Corps Systems Command (MCSC), Grant No. M67854-06-1-5118.

[1]M. A. Basten and J. H. Booske, J. Appl. Phys. **85**, 6313 (1999).
[2]J. H. Booske, B. D. McVey, and T. M. Antonsen, Jr., J. Appl. Phys. **73**, 4140 (1993).
[3]B. E. Carlsten, L. M. Earley, F. L. Krawczyk, S. J. Russell, J. M. Potter, P. Ferguson, and S. Humphries, Jr., Phys. Rev. ST Accel. Beams **8**, 062001 (2005).
[4]B. E. Carlsten, Phys. Plasmas **9**, 5088 (2002).
[5]B. E. Carlsten, S. J. Russell, L. M. Earley, W. B. Haynes, F. Krawczyk, E. Smirnova, Z.-F. Wang, J. M. Potter, P. Ferguson, and S. Humphries, *Proceedings of the Seventh Workshop on High Energy Density and High Power RF*, 2006, edited by D. K. Abe and G. S. Nusinovich (American Institute of Physics, New York, 2006), Vol. 807, p. 326.
[6]K. T. Nguyen, J. Pasour, E. L. Wright, D. E. Pershing, and B. Levush, *Proceedings of the 10th International Vacuum Electronics Conference*, Rome (IEEE, New York, 2009), p. 298.
[7]P. B. Larsen, D. K. Abe, S. J. Cooke, B. Levush, T. M. Antonsen, and R. E. Myers, *Proceedings of the 10th International Vacuum Electronics Conference* (IEEE, New York, 2009), p. 225.
[8]Y.-M. Shin, L. R. Barnett, and N. C. Luhmann, Jr., IEEE Trans. Electron Devices **56**, 706 (2009).
[9]Y. M. Shin, J. K. So, K. H. Jang, J. H. Won, A. Srivastava, and G. S. Park, Appl. Phys. Lett. **90**, 031502 (2007).
[10]A. G. Bailey, E. I. Smirnova, L. M. Earley, B. E. Carlsten, and J. L. Maxwell, Proc. SPIE **6120**, 14 (2006).
[11]S. Humphries, S. Russell, B. Carlsten, L. Earley, and P. Ferguson, Phys. Rev. ST Accel. Beams **7**, 060401 (2004).
[12]S. K. Wong, J. S. Kim, J. D. Goldberg, D. H. Edgell, and W. L. Spence, *Proceedings of the 18th Particle Accelerator Conference*, New York, 1999 (IEEE, New York, 1999), p. 1043.
[13]S. J. Russell, Z. F. Wang, W. B. Haynes, R. M. Wheat, B. E. Carlsten, L. M. Earley, S. Humphries, and P. Ferguson, Phys. Rev. ST Accel. Beams **8**, 080401 (2005).
[14]M. A. Basten, J. H. Booshe, and J. Anderson, IEEE Trans. Plasma Sci. **22**, 960 (1994).
[15]B. E. Carlsten, S. J. Russell, L. M. Earley, F. L. Krawczyk, J. M. Potter, P. Ferguson, and S. Humphries, IEEE Trans. Plasma Sci. **33**, 85 (2005).
[16]M. E. Read, G. Miram, R. L. Ives, V. Ivanov, and A. Krasnykh, *Proceedings of the 22nd Particle Accelerator Conference, 2003*, edited by J. Chew, P. Lucas, and S. Webber (IEEE, New York, 2003), p. 1137.
[17]J. H. Booske, M. A. Basten, and A. H. Kumbasar, Phys. Plasmas **1**, 1714 (1994).
[18]A. Burke, V. Besong, and K. Granlund, *Proceedings of the Seventh International Vacuum Electronics Conference*, Monterey, 2006 (IEEE, New York, 2006), p. 485.
[19]See National Technical Information Service Document No. DE2006876449 (G. Scheitrum, "Design and construction of a W-band sheet beam klystron," Report No. Slac-pub-11688, 2006). Copies may be ordered from National Technical Information Service, Springfield, VA.
[20]G. Scheitrum, G. Caryotakis, A. Burke, A. Jensen, E. Jongewaard, M. Neubauer, R. Phillips, and R. Steele, *Proceedings of the Seventh International Vacuum Electronics Conference*, Monterey, 2006 (IEEE, New York, 2006), p. 481.
[21]H. C. Kirbie and H. T. Hawkins, *Proceedings of the 14th IEEE International Pulsed Power Conference (PPC-2003)*, Dallas, 2003, edited by M. Giesselmann and A. Neuber (IEEE, Nuclear and Plasma Sciences Society, New York, 2003), Vol. 1, p. 13.
[22]Y. M. Shin, L. R. Barnett, and N. C. Luhmann, Jr., IEEE Trans. Electron Devices **56**, 3196 (2009).
[23]R. L. Ives, A. Attarian, T. M. Read, J. Davis, H. Tran, W. J. Tallis, S. Davis, S. E. Gadson, N. Blach, D. Brown, and E. Kiley, IEEE Trans. Electron Device **56**, 753 (2009).
[24]MAXWELL3D user's guide. Ansoft Corp., 225 West Station Square Drive, Pittsburgh, PA 15219, USA (online) available: http://www.ansoft.com/products/em/maxwell/.
[25]CST Simulation Technology, Bad Nauheimer Str. 19 64289 Darmstadt, Germany (online) available: http://www.cst.com/Content/Products/PS/Overview.aspx.
[26]TRAK, Field Precision Inc., P.O. Box 13595, Albuquerque, NM 87192, USA (online) available: http://www.fieldp.com/beams.html.
[27]For additional information see: http://dx.doi.org/10.1063/1.3383053 for S. Humphries, Field Precision, 2009 "Tutorial: Simulating a planar electron-beam gun with OMNITRAK" and "Tutorial: Representing cathode temperature effects in electron gun codes."